Element-Specific Curie Temperatures and Heisenberg Criticality in Ferrimagnetic Gd₆(Mn_{1-x}Fe_x)₂₃

Temperature-dependent X-ray magnetic circular dichroism solves a long-standing puzzle of non-monotonic Curie temperatures coupled to monotonic composition-controlled magnetization.

any rare-earth (R)-transitionmetal (M, M') ternary alloys of the type $R_a(M_{1-x}M'_x)_b$ exhibit non-monotonic ferrimagnetic Curie temperatures ($T_{\rm C}$) coupled to monotonic composition-controlled magnetization. Its origin has remained an important long-standing puzzle in the absence of studies investigating their temperature (*T*)-dependent element-specific magnetism. To answer this question, a team of scientists from the NSRRC, Taiwan, and Institut Jean Lamour, France, conducted a systematic study of the ferrimagnetic series $Gd_6(Mn_{1-x}Fe_x)_{23}$, x = 0.0-0.75. The researchers used the experimental techniques of X-ray absorption spectroscopy (XAS), X-ray magnetic circular dichroism (XMCD), and hard X-ray photoemission spectroscopy (HAXPES) in combination with density functional theory calculations, including on-site Coulomb energy (DFT+U), to determine the answer. For the first time, the researchers successfully applied the Kouvel-Fisher analysis method to elementspecific *T*-dependent XMCD data. The study unambiguously revealed distinct sublattice $T_{\rm C}$ values and 3-D Heisenberg critical behavior of the ferrimagnetic transition in $Gd_6(Mn_{1-x}Fe_x)_{23}$, as well as clarified the origin of non-monotonic ferrimagnetic $T_{\rm C}$ coupled to monotonic composition-controlled magnetization.1

As shown in **Figs. 1(a)–1(f)**, the researchers performed XAS–XMCD measurements at the Dragon beamline **TLS 11A1**, with an applied field of ± 1 T for the series $Gd_6(Mn_{1-x}Fe_x)_{23}$, x=0.0-0.75 after characterization of the

crystal structure and ferrimagnetic $T_{\rm C}$ values obtained from magnetization measurements. Figures 1(a)-1(c)show representative XAS spectra for (a) Gd M-edge and (b) Mn L-edge of the parent compound, as well as (c) the Fe L-edge of $Gd_6(Mn_{0.5}Fe_{0.5})_{23}$ measured at T = 29 K. From such measurements of compounds with x = 0.0-0.75, the researchers obtained XMCD spectra, as shown for all x in panels (d) to (f). While the Gd M-edge XMCD spectra for all x indicate a total magnetic moment of ~7 μ_B , the Mn L-edge XMCD shows a small net magnetic moment (~0.4 μ_B), which switches from parallel to antiparallel with respect to the Gd magnetic moments and becomes $\sim 0.05 \,\mu_B$ on increasing x. By contrast,

Fe L-edge XMCD shows that Fe magnetic moments are antiparallel with respect to the Gd magnetic moments for all x and increase systematically from $\sim\!0.4~\mu_B$ (for x = 0.2) to 1.4 μ_B (for x = 0.75).

Next, the researchers performed HAXPES measurements at **SP 12U1**, one of the Taiwan-contract Beamlines in SPring-8, for the series and showed that the Gd 3*d* core-level multiple spectra can be analyzed using an intermediate coupling scheme.² By contrast, the Fe 2*p* core-level spectra showed single peaks attributed to typical metals, whereas the Mn 2*p* spectra showed a main peak and shoulder, which could be assigned to Mn up-spin and down-spin sites.

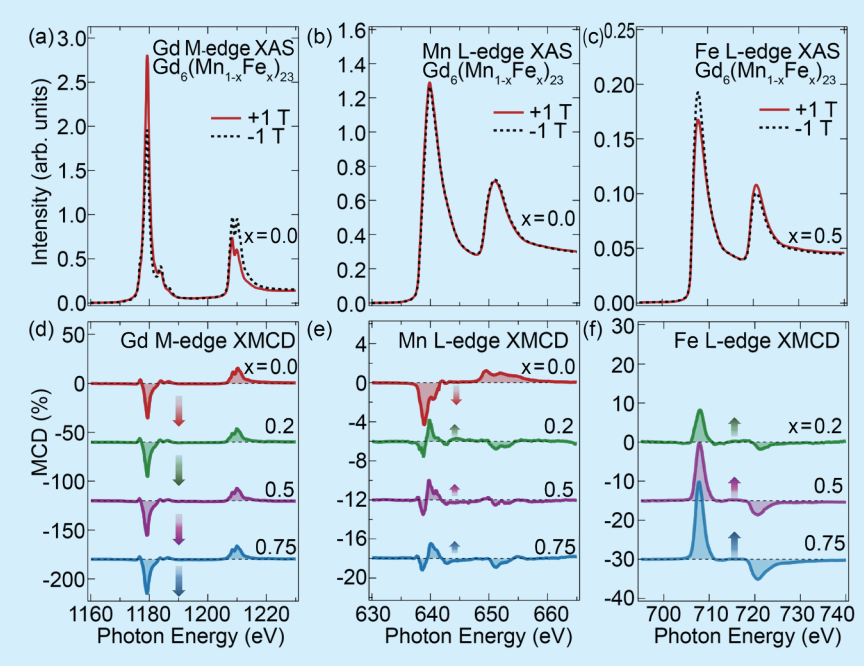


Fig. 1: Representative XAS spectra of $Gd_6(Mn_{1-x}Fe_x)_{23}$ with an applied field of ± 1 T for (a) Gd M-edge (x = 0), (b) Mn L-edge (x = 0), and (c) Fe L-edge (x = 0.5) measured at T=29 K, from which we obtained the XMCD spectra, as shown for all x in panels (d)–(f). XAS–XMCD spectra of (d) Gd M-edge, (e) Mn L-edge, and (f) Fe L-edge of the series $Gd_6(Mn_{1-x}Fe_x)_{23}$ (x = 0, 0.2, 0.5, and 0.75) measured at T=29 K. Arrows in (d)–(f) show the relative magnitude and orientation of the spins. [Reproduced from Ref. 1]

This observation is consistent with the crystal and magnetic structures of the parent Gd₆Mn₂₃, as obtained from neutron diffraction studies,³ which indicated two types of Mn "b, d" upspin sites and two types of Mn "f₁, f₂" down-spin sites, as shown in **Fig. 2(a)**. The Fe and Mn 3s core level HAXPES spectra showed exchange splitting, and a Van–Vleck analysis result indicated magnetic moments that are consistent with neutron diffraction results.²

Next, the researchers conducted bulk-sensitive HAXPES valence band spectroscopy and compared it with DFT+U electronic structure calculations. Figure 2(b) shows the comparison between the experimental valence band spectrum and the calculated partial density of states (P-DOS) for Gd 4f, Gd 5d, Mn 4s, and Mn 3d and the total DOS for Gd₆Mn₂₃ obtained from DFT+U calculations with on-site Coulomb energies $U_{Mn}^{DFT} = 0.75 \text{ eV}$ and $U_{Gd}^{DFT} =$ 6.5 eV. The optimal values of U_{Mn}^{DFT} = 0.75 eV and U_{Gd}^{DFT} = 6.5 eV also yielded magnetic moment values consistent with neutron diffraction results.3 The crucial role of on-site Coulomb energies in the valence band states of transition metals was further clarified by 2p-3d resonant-PES.4 Figure 2(c) shows a plot of the valence band P-DOS for Gd 4f, Gd 5d, Fe 4s, and Fe 3d and the total DOS for Gd₆Fe₂₃ obtained from the DFT+U calculations. To compare with experimental data for x =0.75, the calculated total DOS for $Gd_6(Mn_{0.25}Fe_{0.75})_{23}$ was approximated as a sum of 25% Gd₆Mn₂₃ and 75% Gd₆Fe₂₃ total DOS, plotted together with the bulk-sensitive HAXPES valence band spectrum in Fig. 2(d). The results indicated a fair match between experimental and calculated results.1

The researchers conducted T-dependent XMCD and bulk magnetization experiments to determine element-specific T_C values and the nature of the ferrimagnetic transition in $Gd_6(Mn_{1-x}Fe_x)_{23}$.

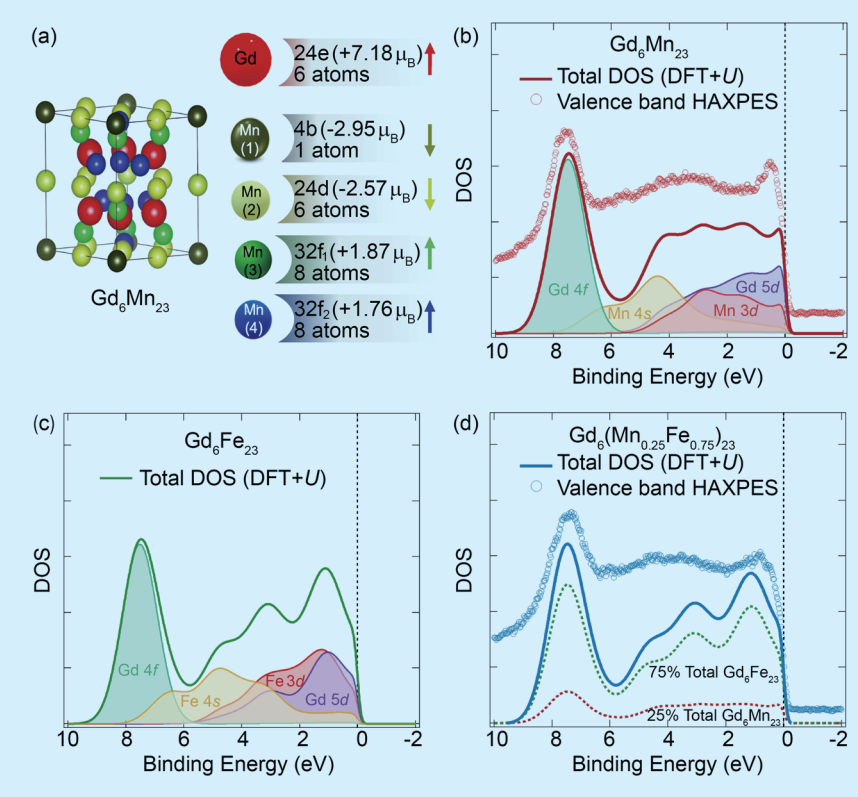


Fig. 2: Crytal structure schematic and comparison of HAXPES valence band with DOS calculations. (a) The crystal structure of Gd₆Mn₂₃, indicating the magnetic moments from the band structure calculations of the Gd site, Mn "b, d" sites, and Mn "f₁, f₂" sites. (b) The P-DOS for Gd 4f, Gd 5d, Mn 4s, and Mn 3d and the total DOS for Gd₆Mn₂₃ obtained from DFT+U calculations with $U_{m}^{DFT} = 0.75$ eV and $U_{Gd}^{DFT} = 6.5$ eV compared with bulk-sensitive HAXPES valence band spectrum. (c) The valence band P-DOS for Gd 4f, Gd 5d, Fe 4s, and Fe 3d and the total DOS for Gd₆Fe₂₃ obtained from DFT+U calculations. (d) The valence band total DOS for Gd₆(Mn_{0.25}Fe_{0.75})₂₃ is approximated by an additive mixture of 25% Gd₆Mn₂₃ and 75% Gd₆Fe₂₃ total DOS, and it is plotted together with the bulk-sensitive HAXPES valence band spectrum. [Reproduced from Ref. 1]

Figure 3 (see next page) shows the T-dependent Gd/Fe XMCD results fitted to a power law for all x. The data revealed that Gd T_C = 273.5 K for x = 0.0 and 0.75 and that it was smaller than the bulk $T_{\rm C}$ values (489 K for x = 0; 306 K for x = 0.75). In contrast, it decreased to the bulk $T_{\rm C}$ values of 172 K (for x = 0.2) and 135 K (for x =0.5) when Gd $T_{\rm C}$ decreased to below 273.5 K. A scaling analysis (Fig. **3(b)**) indicated a 3D Heisenbergtype transition for all x values. To confirm the critical behavior, a more rigorous Kouvel-Fisher analysis was performed for all x values, and the results are shown in the bottom row of **Fig. 3**. The *T*-dependent Mn L-edge XMCD could not be measured as it showed weak XMCD intensity. The results confirmed the 3-D Heisenberg critical behavior of the ferrimagnetic transition in Gd₆(Mn_{1-x}Fe_x)₂₃.1

Finally, a magnetic phase diagram (Fig. 4, see next page) based on element-specific $T_{\rm C}$ values with total magnetization from XMCD and total bulk magnetization measurements $(M_{Tot}^X \text{ and } M_{Tot}^B, \text{ respectively})$ showed three regions with (i) Mnsublattice bulk- $T_{\rm C}$ > Gd-sublattice $T_{\rm C}$, (ii) a reduced common- $T_{\rm C}$ for all sublattices, and (iii) Fe-sublattice bulk- $T_{\rm C}$ > Gd-sublattice $T_{\rm C}$. The results thus revealed that the Mnmoment switching and gradual increase in Fe moment combined to cause non-monotonic T_C values coupled to monotonic magnetization. The study indicates the importance of element-specific $T_{\rm C}$ values for tuning magnetic properties in R_a(M_{1-x}M'_x)_b ternary alloys. (Reported by Ashish Chainani)

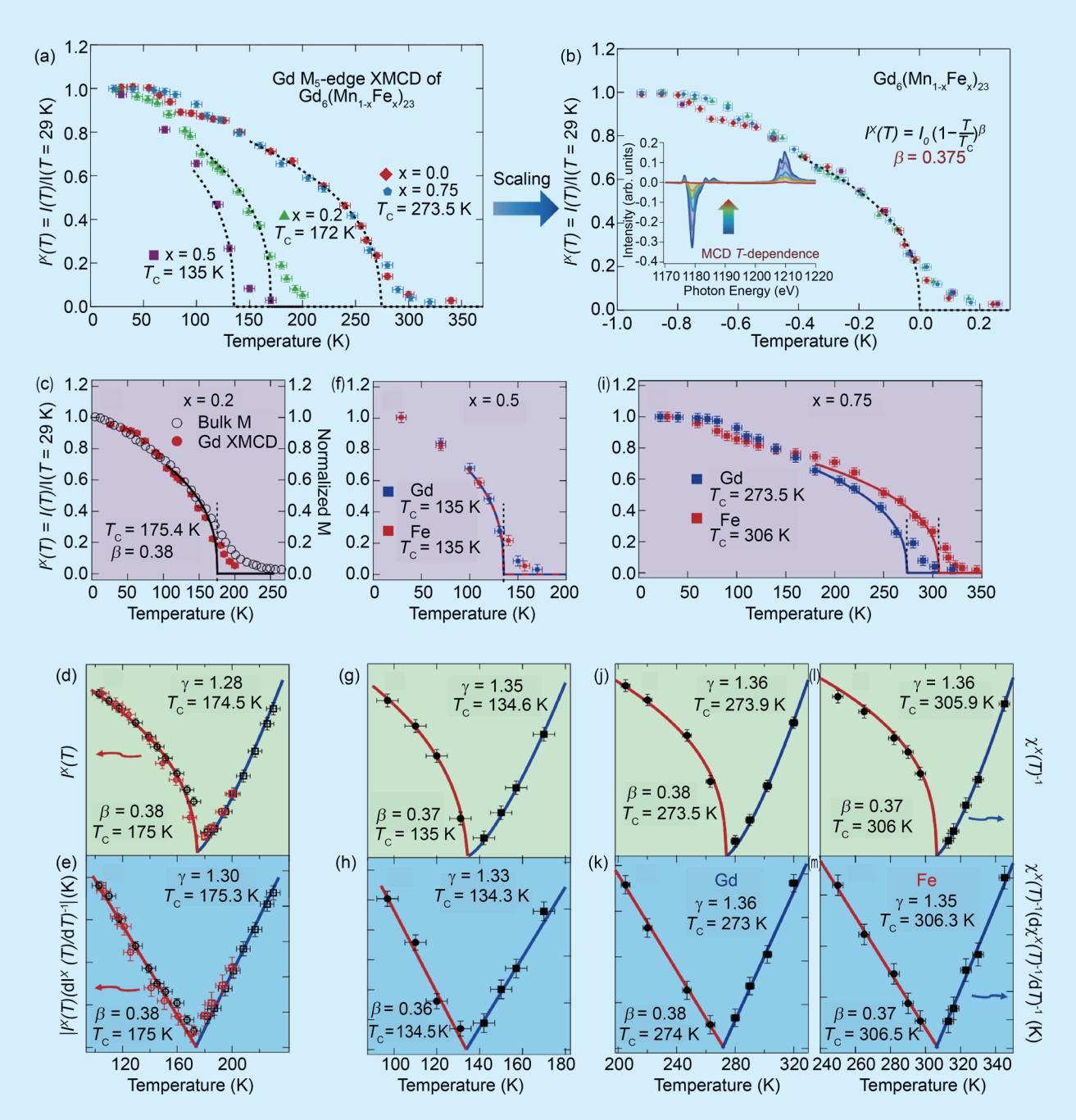


Fig. 3: Element-specific $T_{\rm C}$ values from power law analyses and Kouvel–Fisher analyses of XMCD. (a) T dependence of the Gd M₅-edge XMCD intensity for Gd₆(Mn_{1-x}Fe_x)₂₃, fitted by a power law exponent $\beta = 0.38 \pm 0.01$ (dashed black line). (b) Critical scaling behavior for the Gd₆(Mn_{1-x}Fe_x)₂₃ series. The inset shows T dependence of Gd M-edge XMCD intensity for Gd₆(Mn_{0.2}Fe_{0.75})₂₃. (c) T dependence of the Gd M₅-edge XMCD intensity and total bulk magnetization ($M_{Bot}^B(T)$) of Gd₆(Mn_{0.8}Fe_{0.2})₂₃ fitted by a power law with $\beta = 0.38 \pm 0.01$ (black line). (d) Power-law and (e) Kouvel–Fisher analysis fits for $M_{Bot}^B(T)$ (black empty circles). The Gd M₅-edge XMCD intensity $I^X(T)$ plotted together (red empty circles) also follows the Kouvel–Fisher analysis for $M_{Bot}^B(T)$ near $T_{\rm C}$. (f) T dependence of the Gd M₅-edge (blue squares) and Fe L₃-edge (red squares) XMCD intensity for Gd₆(Mn_{0.5}Fe_{0.5})₂₃ fitted to a power law with $\beta = 0.37 \pm 0.01$ (dashed blue-red line). (g) Power-law and (h) Kouvel–Fisher analyses for both Gd M₅-edge and Fe L₃-edge XMCD intensities plotted together. (i) T dependence of the Gd M₅-edge (blue squares) and Fe L₃-edge (red squares) XMCD intensity for Gd₆(Mn_{0.2}Fe_{0.75})₂₃ fitted by a power law with $\beta = 0.38 \pm 0.01$ (blue and red lines, respectively). (j) Power-law and (k) Kouvel–Fisher analyses for Gd M₅-edge XMCD intensities, and (l) power-law and (m) Kouvel–Fisher analyses for Fe L₃-edge XMCD intensities. The red and blue lines in (d), (e), (g), (h), (j)–(m) are the fits below and above $T_{\rm C}$, respectively. All XMCD results were obtained with an applied field of ±1 T. [Reproduced from Ref. 1]

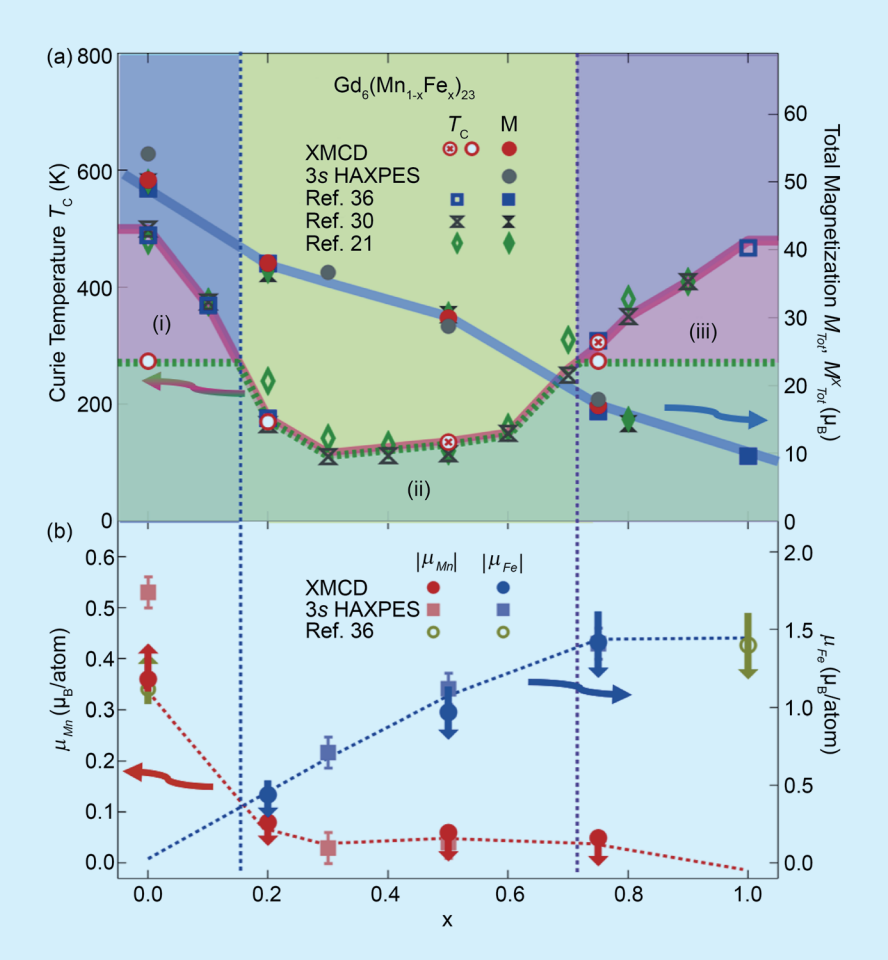


Fig. 4: Magnetic phase diagram of Gd₆(Mn_{1-x}Fe_x)₂₃. (a) Summary of element-specific $T_{\rm C}$ values with XMCD and bulk magnetizations ($M_{\rm Tot}^{\rm X}$ and $M_{\rm Tot}^{\rm B}$) as a function of x. The plots of $T_{\rm C(Gd)}$ (empty red circle O) and $T_{\rm C(Fe)}$ (red cross circle ⊗) show three regions: (i) For 0.0 < x ≤ 0.15, bulk $T_{\rm C}$ is determined by the Mn sublattice, and $T_{\rm C(Gd)}$ = 273.5 K < bulk $T_{\rm C}$. (ii) For 0.15 < x ≤ 0.72, the Gd and Fe sublattices show the same $T_{\rm C}$ = bulk $T_{\rm C}$. (iii) For 0.72 < x ≤ 1.0, the Fe moments determine the bulk $T_{\rm C}$, and $T_{\rm C(Gd)}$ = 273.5 K < bulk $T_{\rm C}$. (b) Summary of Mn and Fe magnetic moments (μ_{Mn} , μ_{Fe}) as a function of x, showing switching of Mn moments for x ≥ 0.2 plotted with magnetic moments from 3s HAXPES analysis. [Reproduced from Ref. 1]

This report features the work of Ashish Chainani and his collaborators published in Commun. Mater. 5, 68 (2024) and Physical Review B 109, 035102 (2024).

TLS 11A1 (Dragon) MCD, XAS SP 12U1 HAXPES/Photoemission

- XAS, XMCD, HAXPES
- Ferrimagnetic Transition, Materials Science, Condensed-matter Physics

References

- T. Ly Nguyen, T. Mazet, E. Gaudry, D. Malterre, F.-H. Chang, H.-J. Lin, C.-T. Chen, Y.-C. Tseng, A. Chainani, Commun. Mater. 5, 68 (2024).
- T. Ly Nguyen, T. Mazet, D. Malterre, H. J. Lin, M. Yoshimura, Y. F. Liao, H. Ishii, N. Hiraoka, Y. C. Tseng, A. Chainani, Phys. Rev. B 106, 045144 (2022).
- 3. A. Delapalme, J. Déportes, R. Lemaire, K. Hardman, W. J. James, J. Appl. Phys. **50**, 1987 (1979).
- 4. T. Ly Nguyen, C.-C. Yang, C.-H. Wang, Y.-W. Yang, T. Mazet, E. Gaudry, D. Malterre, M. Yoshimura, Y. F. Liao, H. Ishii, N. Hiraoka, H. J. Lin, Y. C. Tseng, A. Chainani, Phys. Rev. B **109**, 035102 (2024).

Unlocking Dual Topological States in the 2D Limit

A promising way enhances the understanding of 2D topological materials and lays the groundwork for future electronic and superconducting applications.

Two-dimensional (2D) quantum materials have gained attention for their exceptional electronic properties, particularly in spintronics and quantum computing. Among them, 2D topological insulators (TIs) are notable for their protected metallic edge states, which exhibit spin-momentum locking and insusceptibility to backscattering from nonmagnetic impurities. These features make them strong candidates for low-power electronic devices and quantum computing. The discovery of topological nodal line semimetals (TNLSMs), which host one-dimensional nodal lines of band degeneracy in the Brillouin zone, has further expanded the landscape of topological materials. However, experimental realization of 2D TNLSMs remains rare despite numerous theoretical predictions. Stanene, the monolayer allotrope of tin (Sn), has emerged as a promising 2D TI because of its sizable topological band gap (~0.3 eV) induced by strong spin-orbit coupling (SOC). Unlike silicene and germanene, which possess much smaller SOC-induced gaps, stanene's robust band inversion enables the quantum spin Hall effect at room temperature. Additionally, stanene's electronic properties can be tuned *via* strain